

Two-photon lithography for 3D magnetic nanostructure fabrication

Gwilym Williams^{1,§}, Matthew Hunt^{1,§}, Benedikt Boehm², Andrew May¹, Michael Taverne³, Daniel Ho³, Sean Giblin¹, Dan Read¹, John Rarity³, Rolf Allenspach², and Sam Ladak¹ (✉)

¹ School of Physics and Astronomy, Cardiff University, Cardiff CF24 3AA, UK

² IBM Research - Zurich, Säumerstrasse 4, 8803 Rüschlikon, Switzerland

³ Department of Electrical and Electronic Engineering, University of Bristol, Bristol BS8 1UB, UK

[§] Gwilym Williams and Matthew Hunt contributed equally to this work.

Received: 14 March 2017

Revised: 8 May 2017

Accepted: 27 May 2017

© The author(s). This article is published with open access at link.springer.com

KEYWORDS

magnetism,
spintronics,
nanomagnetism,
three-dimensional (3D)
lithography

ABSTRACT

Ferromagnetic materials have been utilized as recording media in data storage devices for many decades. The confinement of a material to a two-dimensional plane is a significant bottleneck in achieving ultra-high recording densities, and this has led to the proposition of three-dimensional (3D) racetrack memories that utilize domain wall propagation along the nanowires. However, the fabrication of 3D magnetic nanostructures of complex geometries is highly challenging and is not easily achieved with standard lithography techniques. Here, we demonstrate a new approach to construct 3D magnetic nanostructures of complex geometries using a combination of two-photon lithography and electrochemical deposition. The magnetic properties are found to be intimately related to the 3D geometry of the structure, and magnetic imaging experiments provide evidence of domain wall pinning at the 3D nanostructured junction.

1 Introduction

Current information technologies rely on growth and processing techniques that allow the fabrication of two-dimensional nanostructures [1]. Currently, this involves the exposure of a photoresist to light through a mask to generate a nanoscale pattern, which is subsequently transferred onto another material via deposition or etching processes [1].

On one hand, the increasing demand for higher

data storage densities while maintaining short access times has recently generated an interest in three-dimensional (3D) data storage solutions such as magnetic racetrack memory [2]. On the other hand, the experimental and theoretical study of 3D magnetic nanostructures is of fundamental interest and has recently allowed the probing of new and exciting physics such as Bloch point domain wall propagation [3], curvature induced effective Dzyaloshinskii–Moriya interaction [4], and magnetic charge transport in 3D

Address correspondence to LadakS@cardiff.ac.uk

artificial spin-ice structures [5]. These studies require alternative fabrication strategies to realize very simple 3D geometries. A common approach to fabricate 3D magnetic nanostructures is to electrodeposit a magnetic material into alumina templates or ion-track-etched templates. This is a promising route because electrodeposition is a well-established method for growing a range of magnetic materials [6] and has allowed the fabrication and characterization of cylindrical magnetic nanowires [3, 7]. More recently, ion-track-etched templates have also been used to fabricate interconnected networks of NiCo nanowires [8]. Unfortunately, the technique does not currently allow the fabrication of predesigned complex 3D geometries. Focused electron beam deposition is a powerful technique that has allowed the fabrication of 3D magnetic nanostructures, yielding geometries such as wires and helices [9]. This method can be used to fabricate a range of magnetic materials [9] and has also recently led to structures with measurable magneto-optical Kerr effect signals [10]. However, the deposited material has often been contaminated with large amounts (> 5%) of carbon and oxygen. It is also difficult to envisage the fabrication of complex, extended 3D networks or geometries using this technique. In other disciplines, a range of self-assembly and chemical methods have resulted in great success in the fabrication of 3D nano/microstructures, including chiral liquid crystal structures [11, 12] and hybrid 3D graphene/gold nanoparticle structures [13]. In addition, the manipulation of droplets upon surfaces via magnetic guiding and three-phase contact lines has been shown to be a powerful method to produce 3D microstructures in a number of geometries, including magnetic inks [14], CdTe quantum dots [15], silver nanoparticles [15], and manganese chloride salts [15].

Two-photon lithography (TPL) [16] is a relatively new technique that has largely been exploited by the metamaterials and microfluidic communities to fabricate complex 3D nanostructured materials. In this technique, a femtosecond laser operating in the infra-red (typically $\lambda \approx 780$ nm) is focused to a diffraction-limited spot within a conventional photoresist. The high peak intensity at the focal point allows simultaneous absorption of two photons to excite the electronic

transition within the photoinitiator molecule, causing polymerization or depolymerization of the resist. This non-linear optical process is proportional to the square of the intensity, and thus only occurs within the central region of the focal spot. By translating the point of focus within the resist, 3D nanostructures of arbitrary geometry can be produced. The technique can be used to fabricate 3D nanostructures within a polymer or to realize metallic nanostructures by employing surfactant-assisted multiphoton-induced reduction [17].

In this study, we utilize a novel fabrication approach, which uses a combination of TPL and electrodeposition, to fabricate complex 3D Co magnetic nanostructures, by design. The structures are of high purity and their magnetic properties can be measured using standard surface sensitive techniques such as the magneto-optical Kerr effect (MOKE) and spin-polarized scanning electron microscopy (spin-SEM). Our technique provides a new route to fabricate 3D nanomagnetic elements and wires with desired properties.

2 Results and discussion

An overview of the fabrication procedure is presented in Figs. 1(a)–1(d). A positive photoresist is spin-coated onto a glass/indium tin oxide (ITO) (500 nm) substrate (Fig. 1(a)) and TPL is used to expose a 3D pattern within the resist (Fig. 1(b)). Next, a development process is used to remove the exposed regions of the resist, leaving a series of channels. Electrodeposition is then used to fill the channels with Co (Fig. 1(c)), after which the resist is removed to obtain a 3D magnetic nanostructure (Fig. 1(d)). In order to investigate the possible lateral feature size, arrays of cylinders were fabricated by varying the power and development time. The challenge in fabricating complex 3D geometries within a positive resist is to balance the development time that allows removal of the exposed resist, while minimizing dark erosion, which leads to larger feature sizes. Figure 1(e) shows the variation of the lateral feature size with the laser power for a fixed development time of 30 min. The lateral feature size decreases non-linearly with the laser power and the minimum lateral feature size is found to be approximately 435 nm.

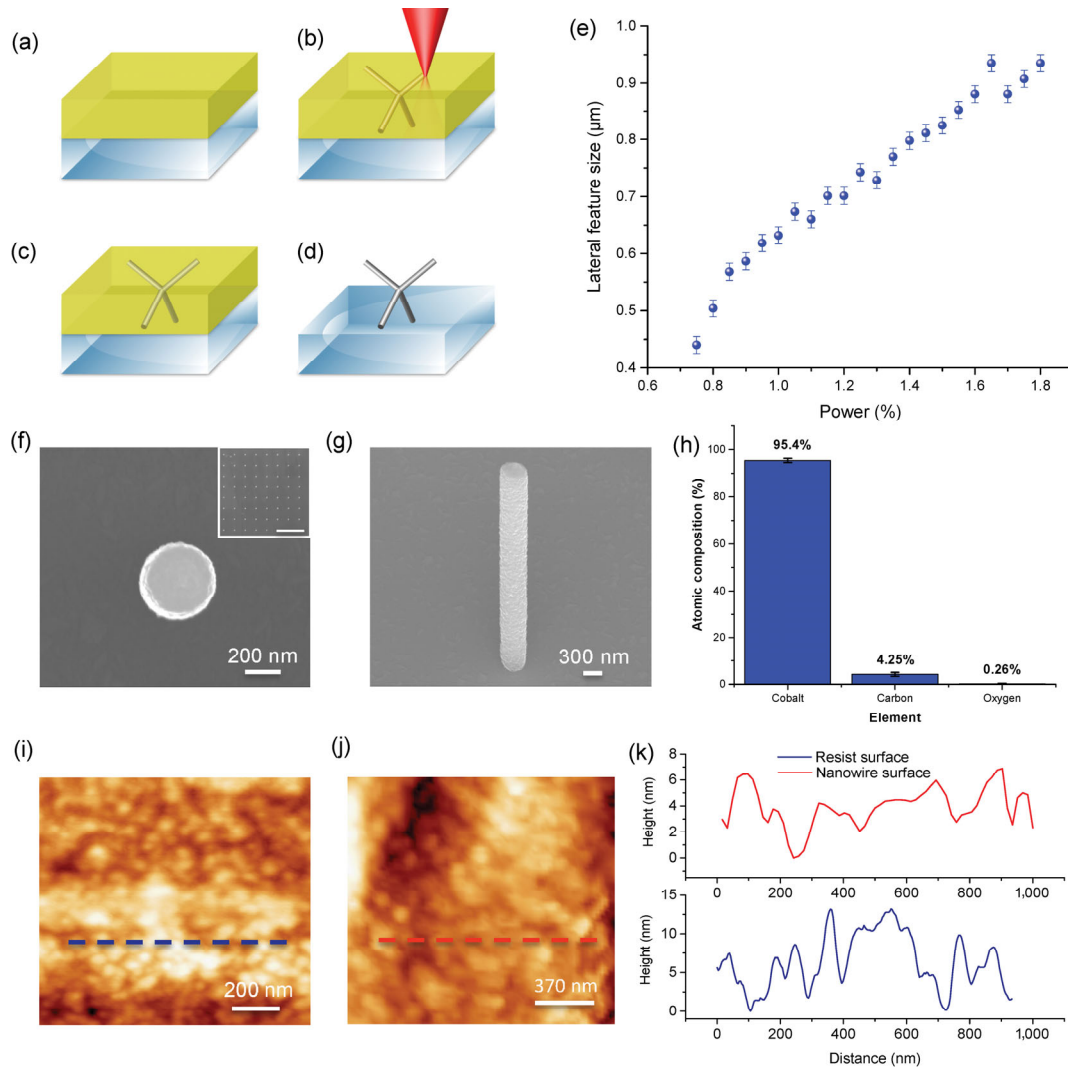


Figure 1 Fabrication and structural characterization of 3D magnetic nanostructures. (a) Spin-coating of a positive resist onto a glass/ITO substrate. (b) Two-photon lithography of a 3D structure into the positive resist. (c) Electrodeposition of Co into the channels. (d) Lift off of the resist. (e) Lateral feature sizes obtained for pillars fabricated at different powers. (f) SEM micrograph of a single 435 nm Co nanowire. Inset: an array of sub-500 nm pillars. Scale bar = 8 μm. (g) SEM micrograph of a single 435 nm Co nanowire captured at a 60° angle. (h) Energy dispersive X-ray analysis of Co pillars. (i) AFM image of the resist channel surface. (j) AFM image of a nanowire sidewall. (k) Profiles obtained from the nanowire sidewall and AFM images of the resist channel (i) and (j).

Simple models of the two-photon lithography process within a positive resist show that the channel diameter D can be expressed by [18]

$$D = w(z) \sqrt{\ln \left[\frac{4C\eta^2 P_{\text{laser}}^2 t}{f\tau(\pi h\nu w^2(z))^2 \ln \frac{M_0}{M_{\text{th}}}} \right]} \quad (1)$$

where z is the distance between the feature and the focal point, $w(z)$ is the beam radius at position z , C is

a factor related to the product generation rate, η is the transmittance of the objective lens, P_{laser} is the incident laser power, t is the processing time, f is the repetition frequency of the laser, τ is the pulse width, ν is the frequency of light, M_0 is the initial concentration of the photoinitiator in the ground state, and M_{th} is the threshold amount of the dissolvable photoinitiator. With our optical parameters (see Methods), this yields a minimum feature size of approximately 280 nm. However, taking a dark erosion rate of ≈ 5 nm per minute [19] into account yields

a feature size of approximately 430 nm, close to the observed value.

Figures 1(f) and 1(g) show SEM images of a 435 nm diameter Co nanowire. The nanowire is well-defined with a circular cross section, a smooth top and is 3 μm in length. The inset of Fig. 1(f) shows that it is straightforward to fabricate large, regular arrays of sub-500 nm nanowires. Energy dispersive X-ray analysis was performed on larger 1 μm structures (in order to minimize the signal from the ITO substrate). Figure 1(h) shows the elemental composition obtained after averaging over ten structures and subtracting a small background from the substrate. The structures are found to be of high purity with a Co composition of >95%. The small amounts of carbon and oxygen detected are due to the SEM process and a small amount of the residual resist.

Surface roughness is an important factor in determining the final properties of magnetic nanostructures. In our structures, there are three surfaces that need to be considered. The surface making contact with the substrate is likely to be limited by the roughness of the underlying surface, as in standard thin films. However, the surface roughness of the channel sidewalls and their impact on the nanowire morphology has not been studied previously. In order to investigate this, in-plane channels within the resist were fabricated by two-photon lithography and their roughness were measured using atomic force microscopy (AFM), as shown in Fig. 1(i). This was compared with the surface roughness of a microwire (diameter $\approx 1.5 \mu\text{m}$) that had fallen, exposing its sidewalls (Fig. 1(j)). We found that the surface roughness of the microwire (3 nm) is very close to that of the channel surface (5 nm). Hence, it is likely that the morphology of the channel sidewalls constrains the edge roughness of the grown nanowires. Finally, the upper surface of the nanowire is likely to be strongly dependent on the electric field line distribution across the channel. Previous studies have already demonstrated, via an active-area density model [20], that current crowding effects can lead to non-uniformities on the upper surfaces of electrodeposited structures. The effect is most pronounced within larger microstructures, where current crowding at the channel edges results in a thicker region at the electrolyte–resist

interface. This is less pronounced in our smallest (430 nm diameter) structures but mildly apparent in medium-sized (600–700 nm) structures, and more pronounced in micrometer-sized structures.

In order to demonstrate the versatility of our technique in fabricating 3D nanomagnetic structures, we have used TPL to fabricate arrays of angled wires and then used this design as a building block to realize complex 3D tetrapod structures. The approach is particularly powerful since it could help understand the switching of a complex 3D magnetic nanostructure in terms of the underlying constituents. Figure 2(a) shows a $\sim 300 \mu\text{m} \times 300 \mu\text{m}$ array of angled wires. The array is well-ordered with no defects and low distribution of wire lengths. High magnification images of the wires are shown in Figs. 2(b) and 2(c). The wires have an elliptical cross section with semi-axes of 660 nm in the substrate plane, 885 nm in the direction perpendicular to the long axis of the wire, a length of $\approx 8 \mu\text{m}$, and are inclined at an angle of 30.5° with respect to the substrate. The elliptical cross section of the wire is due to the geometry of the point spread function at the focal point of the objective, during TPL [21].

Figure 2(d) shows a SEM image of a $300 \mu\text{m} \times 300 \mu\text{m}$ array of 3D tetrapod structures fabricated using parameters similar to those used for fabricating the single wires. The high-magnification SEM images shown in Figs. 2(e) and 2(f) demonstrate that the complex tetrapod geometry has been successfully realized. The wires within the tetrapod structures are approximately 8 μm in length and present an elliptical cross section with semi-axes of 615 nm in the substrate plane and 853 nm in the direction perpendicular to the wire long axis. Before attempting surface magnetometry on the 3D nanostructured samples, it is useful to have some understanding of the underlying domain structure upon the tetrapod surface. Standard magnetic imaging techniques such as magnetic force microscopy (MFM) [22], photoemission electron microscopy (PEEM) [23] and Lorentz microscopy [24] are not well-suited for studying 3D nanostructured samples. Here, we exploit the large depth of focus in spin-SEM to image a 3D nanostructured magnetic sample. Figures 3(a)–3(c) show the topography and the x - and y -components of magnetization, respectively,

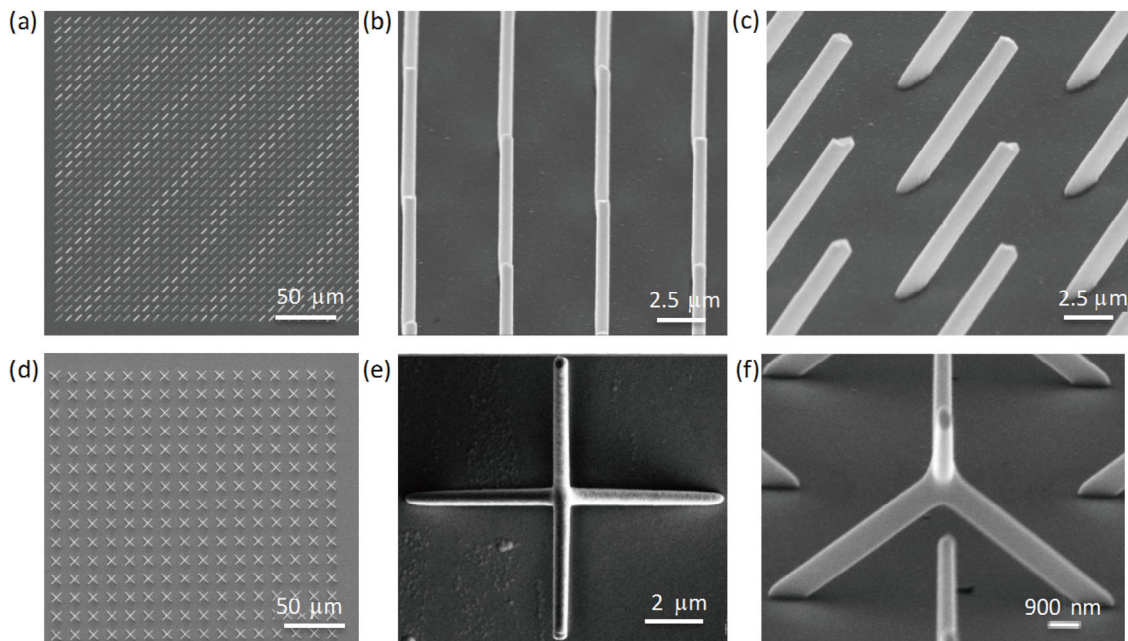


Figure 2 Scanning electron microscopy of 3D magnetic nanostructures. (a) SEM image of a tilted nanowire array (top view). (b) High magnification image of the tilted nanowire array. (c) SEM image of a tilted nanowire array obtained after 90° in-plane rotation. (d) Large scale SEM of a tetrapod array (top view). (e) High-magnification image of a single tetrapod. (f) SEM image of a tetrapod obtained after 45° out-of-plane substrate rotation.

of a single wire within an as-deposited tetrapod structure, obtained by spin-SEM. A schematic representing the x - and y -components using arrows is displayed in Fig. 3(d). Figures 3(e)–3(h) show the same wire after the application of an in-plane pulse with a magnetic flux density of 11.8 mT along the projection of the long axis on to the substrate. The images clearly show that the system is multi-domain both before and after the application of a field, with the remanent magnetization being larger along the long axis of the wire. The demagnetization field perpendicular to the long axis within a tetrapod nanowire is expected to be strong ($0.98\mu_0 M_s = 1.7$ T) and this will result in the magnetization mainly lying parallel to the long axis at remanence, as shown in Fig. 3(g). However, an appreciable angular spread of magnetization direction is observed in Fig. 3(h). Electrodeposited *hcp* Co is also expected to have a uniaxial magnetocrystalline anisotropy directed along its c -axis, with $K_1 = 5.3 \times 10^5$ J/m³. This is approximately a factor of 4 lower than the energy associated with the demagnetization field (2.3×10^6 J/m³). Hence, for randomly oriented crystallites within our wires, we expect the anisotropy term to lead to a distribution of magnetization angles

with respect to the long axis.

MOKE magnetometry has been carried out in the longitudinal geometry upon both sample sets [25]. Figure 4(a) shows a hysteresis loop that was measured with the field along the projection of the wire long axis onto the substrate surface and with an angle of incidence of 14.5° with respect to the wire long axis. The loop displays a steep rise at low fields, which is followed by a slow gradual approach to saturation. The remanence is rather small, around $0.3M_s$, in agreement with published values [26]. Figure 4(b) shows a hysteresis loop measured with the field perpendicular to the projection of the long axis of the wire on to the substrate. The curve strongly resembles that of a hard axis magnetization curve without reaching saturation at 0.5 T, the largest field available in our setup. We infer that the curve is dominated by rotation of the magnetization required to overcome the strong demagnetization field perpendicular to the long axis of the wire, typical of hard axis loops in electrodeposited Co nanowires [27]. It has been reported that electrodeposited nanowires have crystalline grains with a spread in the c -axis direction; however, there is no general agreement on the preferential orientation

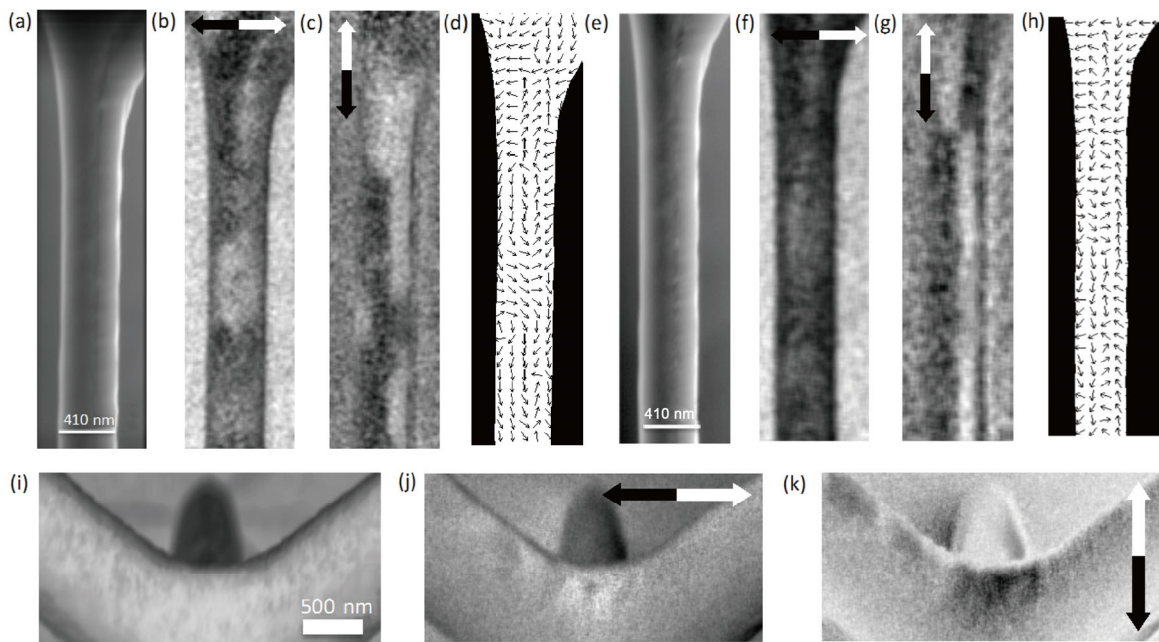


Figure 3 Spin-SEM micrographs of 3D magnetic nanostructures. (a) Absorbed current image of an individual wire within a tetrapod structure. Spin-polarized SEM image showing (b) x - and (c) y -components of magnetization in an as-deposited sample; (d) direction of the in-wire magnetization as deduced from (b) and (c) for the as-deposited sample. (e)–(h) Same sequence as (a)–(d) after a magnetic flux density pulse of 11.8 mT was applied. Spin-SEM micrographs of the vertex area showing magnetization contrast centered on the vertex area; (i) topography, (j) x - and (k) y -components of magnetization.

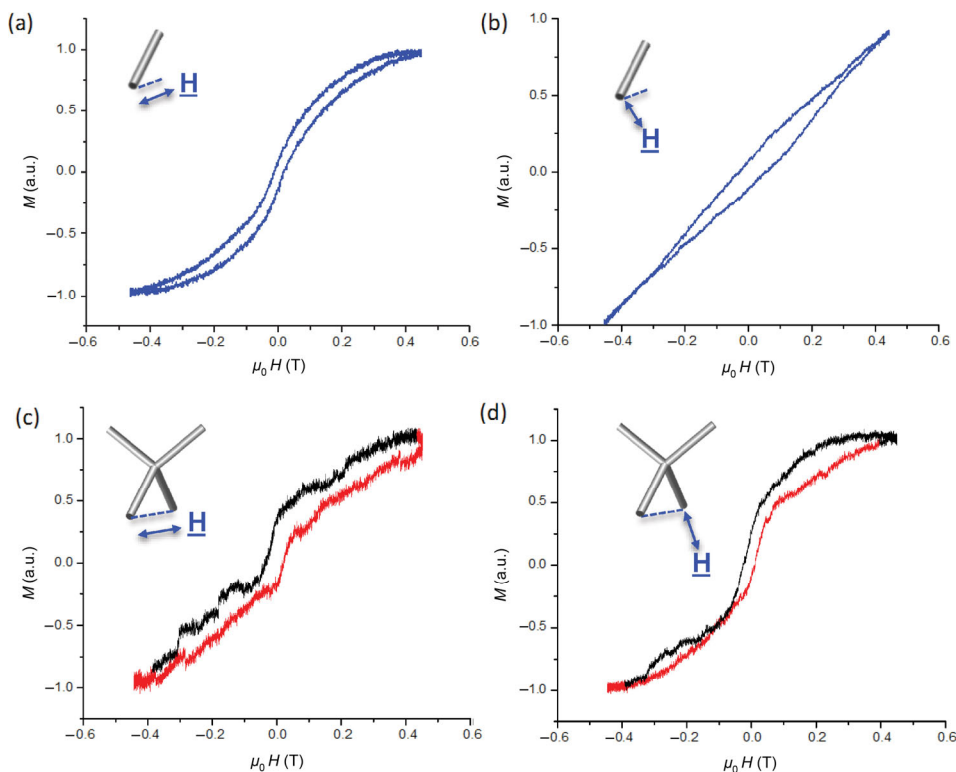


Figure 4 MOKE magnetometry. Longitudinal MOKE loops obtained from (a) single wire array with the field applied along the projection of the wire long axis, (b) single wire array with the field applied perpendicular to the projection of the long axis of the wire, (c) tetrapod array with the field applied along the projection of the lower wires, and (d) tetrapod array with the field applied along the projection of the upper wires.

of the c -axis [26, 27]. Some studies on electrodeposited Co within sulfate-based baths have demonstrated that pH can be an effective means to tune the crystallographic orientation, and hence, magnetocrystalline anisotropy [27]. Figure 4(c) shows the longitudinal MOKE loop obtained from the tetrapod array when the magnetic field is parallel to the projection of the long axes of the lower wires. At low fields, the magnetization displays a much more abrupt switching than that of the single-wire array shown in Fig. 4(a). Further smeared transitions at higher fields can also be discerned. A rather similar loop was obtained when the magnetic field was applied perpendicular to the projection of the lower wires (Fig. 4(d)). The coercivity in this case is observed to be lower than that in Fig. 4(c), but again smaller transitions can be observed at fields above the coercive field.

One can gain some insight into the reversal mechanism within the tetrapods by considering the planar equivalent (sub-micron crosses) of our structures, which have been studied previously [28]. In these samples, nanostructuring was found to play an important role and a complex set of 180° and 90° domain walls was found to form at the vertex area, during the magnetic reversal process. In our tetrapod geometries, a four-way junction is also present; therefore, it appears likely that domain wall pinning at the vertex area will impact the observed magnetometry and may be responsible for multiple switching events. For the tetrapod loop shown in Fig. 4(c), where the field is parallel to the projection of the lower wires, an initial transition (H_{C1}) occurs at a field of 21 mT with only a small variation observed in nominally identical experiments (± 2 mT). This is close to the coercive field observed for single wires (Fig. 4(a)) with the field parallel to the projection of the long axis (17 ± 2 mT). It therefore appears likely that the initial transition observed in Fig. 4(c) is due to the switching of lower wires that have a component parallel to the field, after which the 3D nanostructured vertex impedes domain wall movement into the upper wires. Further transitions are consistently observed above H_{C1} . Here, it is not clear if a domain wall depinning event occurs at the vertex, or if magnetization rotation in the upper wires begins to become significant enough to be observed in the magnetometry. Stochasticity of domain

wall processes is likely to yield a distribution of depinning fields above H_{C1} , as observed in Fig. 4(c).

It is likely that larger structures of similar geometry will not be susceptible to geometric domain wall pinning processes, due to nanostructuring. In order to verify this hypothesis, we fabricated much larger tetrapod structures that have a wire length of approximately $6\ \mu\text{m}$ and an elliptical cross section with semi-axes of $1.5\ \mu\text{m}$ in the substrate plane and $2.75\ \mu\text{m}$ in the direction perpendicular to the long axis of the wire (Figs. S1(a) and S1(b) in the Electronic Supplementary Material (ESM)) and measured their hysteresis loops using MOKE. As expected, the loops exhibit a coercivity similar to that of our smaller nanowires, owing to the flat variation of H_C in nanowires with a diameter above 200 nm [27]. However, additional transitions above the main switching field are not observed, lending credibility to our proposed explanation of magnetometry in smaller structures.

Additional evidence demonstrating the role of the 3D nanostructured vertex in determining the magnetic properties of the smaller structures is observed in spin-SEM images of the vertex obtained at remanence, after the application of a 250 mT field perpendicular to the substrate plane (Figs. 3(i)–3(k)). The images show that, despite the application of a field far above the measured coercive field in the perpendicular direction (27 mT), a complex micro-magnetic configuration consisting of several domain walls are found to remain pinned at the vertex, demonstrating that the local potential landscape has been shaped by the 3D nanostructured geometry.

3 Conclusions

We used two-photon lithography and electrodeposition to fabricate vertical magnetic nanowires, angled magnetic nanowires, and complex 3D tetrapod nanostructures. We have demonstrated that the domain structure within the 3D magnetic nanostructures of complex geometry can be imaged by spin-SEM and standard surface sensitive magnetometry techniques such as MOKE can measure the magnetization reversal upon the 3D nanostructure surface. Shape anisotropy alone cannot explain the shape of the hysteresis loops. It must be concluded that the magnetocrystalline

anisotropy in these polycrystalline Co structures, and in particular, the spread of easy axes determine the domain patterns as well as magnetization switching. Both MOKE and spin-SEM measurements suggest that the 3D nanostructured vertex plays an important role in the magnetization process. Further improvements in the feature size, allowing the fabrication of single domain structures, may be realized using photoresists optimized for deep UV exposure, shorter wavelength lasers [29], and advanced stimulated emission-depletion exposure.

4 Methods

4.1 Fabrication

A positive resist (AZ9260) was spin-coated onto a glass/ITO (700 nm) substrate to obtain a thickness of approximately 6 μm . A two-photon lithography system consisting of a 180 mW, 780 nm laser with a pulse width of 100 fs and repetition rate of 80 MHz was used to write structures within the resist. For the fabrication of samples, the laser power was varied between 3–10.5 mW, the scan speed was varied between 5–20 $\mu\text{m/s}$, and the development time was varied between 15–120 min. After development, electro-deposition was used to fill the channels with Co. A standard Watts bath (600 mL) consisting of cobalt sulfate (90 g), cobalt chloride (27 g), boric acid (14 g), and sodium lauryl sulfate (1 g) was used. A simple two-electrode implementation was used with a Co anode and operated at a constant current of 1 mA. After electrodeposition, the resist was lifted off for 24 h in acetone, after which the samples were subjected to an oxygen plasma treatment for 1 h to remove the residual resist.

4.2 Magnetometry

A 150 mW, 650 nm laser was attenuated to a power of approximately 50 mW, expanded to a diameter of 1 cm, and passed through a Glan–Taylor polarizer to obtain an s-polarized beam. The beam was then focused onto the sample using an achromatic doublet ($f = 30\text{ cm}$), to obtain a spot size of approximately 50 μm^2 . The reflected beam was collected using an achromatic doublet ($f = 10\text{ cm}$) and passed through a second

Glan–Taylor polarizer, from which the transmitted and reflected beams were directed onto two amplified Si photodetectors, yielding the Kerr and reference signals, respectively. A variable neutral density filter was used to ensure that the reference and Kerr signals were of similar values. Subtraction of the reference from the Kerr signal compensates for any change in the laser intensity drift and also eliminates any small transverse Kerr effect from the signal.

4.3 Magnetic Imaging

We employed spin-SEM (also known as SEMP) [30] to investigate the domain patterns in these 3D structures with a high spatial resolution. This technique is an off-spring of standard scanning electron microscopy which is equipped with a spin analyzer. A focused beam of electrons (energy 8 keV) scans along the surface, thereby exciting a wealth of low energy secondary electrons through electron–electron scattering. These electrons (energy 0–20 eV) are ejected into the vacuum and subsequently spin-analyzed. In a ferromagnetic material, the electron spin direction is a direct measure of the magnetization direction in the top 1 nm of the ferromagnet. Because of its high surface sensitivity, the experiment is performed in ultrahigh vacuum ($1 \times 10^{-10}\text{ mbar}$), including the preparation of a clean surface by the removal of nonmagnetic contaminants by mild ion bombardment (Kr^+ ions, 2,000 eV energy). Our setup is capable of simultaneously detecting two magnetization components, e.g., x - and y - components.

4.4 Atomic force microscopy

AFM was carried out on a Bruker Dimension 3000 microscope using commercial atomic force microscopy tips.

Acknowledgements

S. L. gratefully acknowledges funding from EPSRC (Nos. EP/L006669/1, EP/P510750/1, and EP/P511122/1). JGR and Y-LDH acknowledge financial support from the ERC advanced grant 247462 QUOWSS and EPSRC grant EP/M009033/1. The research leading to these results has received funding from the European Union Seventh Framework Programme [FP7-People-2012-ITN]

under grant agreement 316657 (SpinIncur). Information on the data that underpins the research reported here, including how to access them, can be found in the Cardiff University data catalogue at <http://doi.org/10.17035/d.2017.0031438135>.

Electronic Supplementary Material: Supplementary material (scanning electron microscopy and magneto-optical Kerr effect magnetometry of larger micron scale structures) is available in the online version of this article at <https://doi.org/10.1007/s12274-017-1694-0>.

Open Access: This article is distributed under the terms of the Creative Commons Attribution 4.0 International License (<http://creativecommons.org/licenses/by/4.0/>), which permits unrestricted use, distribution, and reproduction in any medium, provided you give appropriate credit to the original author(s) and the source, provide a link to the Creative Commons license, and indicate if changes were made.

References

- [1] Tallents, G.; Wagenaars, E.; Pert, G. Optical lithography: Lithography at EUV wavelengths. *Nat. Photonics* **2010**, *4*, 809–811.
- [2] Parkin, S. S. P.; Hayashi, M.; Thomas, L. Magnetic domain-wall racetrack memory. *Science* **2008**, *320*, 190–194.
- [3] Da Col, S.; Jamet, S.; Rougemaille, N.; Locatelli, A.; Mentès, T. O.; Burgos, B. S.; Afid, R.; Darques, M.; Cagnon, L.; Toussaint, J. C. et al. Observation of Bloch-point domain walls in cylindrical magnetic nanowires. *Phys. Rev. B* **2014**, *89*, 180405.
- [4] Pylypovskiy, O. V.; Sheka, D. D.; Kravchuk, V. P.; Yershov, K. V.; Makarov, D.; Gaididei, Y. Rashba torque driven domain wall motion in magnetic helices. *Sci. Rep.* **2016**, *6*, 23316.
- [5] Shishkin, I. S.; Mistonov, A. A.; Dubitskiy, I. S.; Grigoryeva, N. A.; Menzel, D.; Grigoriev, S. V. Nonlinear geometric scaling of coercivity in a three-dimensional nanoscale analog of spin ice. *Phys. Rev. B* **2016**, *94*, 064424.
- [6] Bicelli, L. P.; Bozzini, B.; Mele, C.; D'Urzo, L. A review of nanostructural aspects of metal electrodeposition. *Int. J. Electrochem. Sci.* **2008**, *3*, 356–408.
- [7] Ivanov, Y. P.; Chuvilin, A.; Vivas, L. G.; Kosel, J.; Chubykalo-Fesenko, O.; Vázquez, M. Single crystalline cylindrical nanowires—Toward dense 3D arrays of magnetic vortices. *Sci. Rep.* **2016**, *6*, 23844.
- [8] da Câmara Santa Clara Gomes, T.; De La Torre Medina, J.; Lemaitre, M.; Piraux, L. Magnetic and magnetoresistive properties of 3D interconnected NiCo nanowire networks. *Nanoscale Res. Lett.* **2016**, *11*, 466.
- [9] De Teresa, J. M.; Fernández-Pacheco, A.; Córdoba, R.; Serrano-Ramón, L.; Sangiao, S.; Ibarra, M. R. Review of magnetic nanostructures grown by focused electron beam induced deposition (FEBID). *J. Phys. D Appl. Phys.* **2016**, *49*, 243003.
- [10] Fernández-Pacheco, A.; Serrano-Ramón, L.; Michalik, J. M.; Ibarra, M. R.; De Teresa, J. M.; O'Brien, L.; Petit, D.; Lee, J.; Cowburn, R. P. Three dimensional magnetic nanowires grown by focused electron-beam induced deposition. *Sci. Rep.* **2013**, *3*, 1492.
- [11] Bisoyi, H. K.; Li, Q. Light-directing chiral liquid crystal nanostructures: From 1D to 3D. *Acc. Chem. Res.* **2014**, *47*, 3184–3195.
- [12] Wang, L.; Li, Q. Stimuli-directing self-organized 3D liquid-crystalline nanostructures: From materials design to photonic applications. *Adv. Funct. Mater.* **2016**, *26*, 10–28.
- [13] Xue, C. M.; Gao, M.; Xue, Y. H.; Zhu, L.; Dai, L. M.; Urbas, A.; Li, Q. Building 3D layer-by-layer graphene–gold nanoparticle hybrid architecture with tunable interlayer distance. *J. Phys. Chem. C* **2014**, *118*, 15332–15338.
- [14] Wang, L. B.; Li, F. Y.; Kuang, M. N.; Gao, M.; Wang, J. X.; Huang, Y.; Jiang, L.; Song, Y. L. Interface manipulation for printing three-dimensional microstructures under magnetic guiding. *Small* **2015**, *11*, 1900–1904.
- [15] Wei, L.; Dong, Z. C.; Kuang, M. X.; Li, Y. N.; Li, F. Y.; Jiang, L.; Song, Y. L. Printing patterned fine 3D structures by manipulating the three phase contact line. *Adv. Funct. Mater.* **2015**, *25*, 2237–2242.
- [16] Sun, H.-B.; Kawata, S. Two-photon photopolymerization and 3D lithographic microfabrication. In *NMR-3D Analysis Photopolymerization. Advances in Polymer Science*; Fatkullin, N.; Ikehara, T.; Jinnai, H.; Kawata, S.; Kimmich, R.; Nishi, T.; Nishikawa, Y.; Sun, H.-B., Eds.; Springer: Berlin Heidelberg, 2004; pp169–273.
- [17] Cao, Y. Y.; Takeyasu, N.; Tanaka, T.; Duan, X. M.; Kawata, S. 3D metallic nanostructure fabrication by surfactant-assisted multiphoton-induced reduction. *Small* **2009**, *5*, 1144–1148.
- [18] Cao, Z. H.; Zheng, M. L.; Dong, X. Z.; Jin, F.; Zhao, Z. S.; Duan, X. M. Two-photon nanolithography of positive photoresist thin film with ultrafast laser direct writing. *Appl. Phys. Lett.* **2013**, *102*, 201108.
- [19] MicroChemicals. *Development of photoresists* [Online]. <http://www.microchemicals.com> (accessed Mar 14, 2017).
- [20] Mehdizadeh, S.; Dukovic, J. O.; Andricacos, P. C.; Romankiw,

- L. T.; Cheh, H. Y. The influence of lithographic patterning on current distribution: A model for microfabrication by electrodeposition. *J. Electrochem. Soc.* **1992**, *139*, 78–91.
- [21] Klar, T. A.; Wollhofen, R.; Jacak, J. Sub-Abbe resolution: from STED microscopy to STED lithography. *Phys. Scr.* **2014**, *2014*, 014049.
- [22] Ivanov, Y. P.; Vivas, L. G.; Asenjo, A.; Chuvilin, A.; Chubykalo-Fesenko, O.; Vázquez, M. Magnetic structure of a single-crystal hcp electrodeposited cobalt nanowire. *Europhys. Lett.* **2013**, *102*, 17009.
- [23] Anders, S.; Padmore, H. A.; Duarte, R. M.; Renner, T.; Stammer, T.; Scholl, A.; Scheinfein, M. R.; Stöhr, J.; Séve, L.; Sinkovic, B. Photoemission electron microscope for the study of magnetic materials. *Rev. Sci. Instrum.* **1999**, *70*, 3973–3981.
- [24] De Graef, M. Recent progress in Lorentz transmission electron microscopy. *ESOMAT* **2009**, 01002.
- [25] Zvezdin, A. K.; Kotov, V. A. *Modern Magneto-optics and Magneto-optical Materials*; CRC Press: Boca Raton, 1997.
- [26] Pirola, K. R.; Béron, F.; Zanchet, D.; Rocha, T. C. R.; Navas, D.; Torrejón, J.; Vazquez, M.; Knobel, M. Magnetic and structural properties of fcc/hcp bi-crystalline multilayer Co nanowire arrays prepared by controlled electroplating. *J. Appl. Phys.* **2011**, *109*, 083919.
- [27] Henry, Y.; Ounadjela, K.; Piroux, L.; Dubois, S.; George, J. M.; Duvail, J. L. Magnetic anisotropy and domain patterns in electrodeposited cobalt nanowires. *Eur. Phys. J. B* **2001**, *20*, 35–54.
- [28] Xu, Y. B.; Vaz, C. A. F.; Hirohata, A.; Yao, C. C.; Lee, W. Y.; Bland, J. A. C.; Rousseaux, F.; Cambril, E.; Launois, H. Domain wall trapping probed by magnetoresistance and magnetic force microscopy in submicron ferromagnetic wire structures. *J. Appl. Phys.* **1999**, *85*, 6178–6180.
- [29] Mueller, P.; Thiel, M.; Wegener, M. 3D direct laser writing using a 405 nm diode laser. *Opt. Lett.* **2014**, *39*, 6847–6850.
- [30] Allenspach, R. Spin-polarized scanning electron microscopy. *IBM J. Res. Dev.* **2000**, *44*, 553–570.

